

Inertial effects in shear flow of a fluid-particle mixture: Resolved simulationsGedi Zhou^{1,*} and Andrea Prosperetti^{2,3,1,†}¹*Department of Mechanical Engineering, Johns Hopkins University, Baltimore, Maryland 21218, USA*²*Department of Mechanical Engineering, University of Houston, 4726 Calhoun Rd, Houston, Texas 77204-4006, USA*³*Faculty of Science and Technology and J.M. Burgers Centre for Fluid Dynamics, University of Twente, P.O. Box 217, 7500 AE Enschede, The Netherlands*

(Received 14 February 2020; accepted 26 June 2020; published 10 August 2020)

This paper presents results of the resolved simulation of particles suspended in a fluid in shear flow. Unlike most of the existing work on this subject, the ratio of the particle density to that of the suspending fluid is not 1 but varies between 2.5 and 10, with a focus on inertial effects rather than gravity, which is not considered. Two particle Reynolds numbers are considered, 20 and 40, while the average particle volume fraction varies from 5% to 33%. The study focuses on the effects of inertia on this class of flows. It is shown that the memory of the particles' earlier state of motion associated with inertia is responsible for significant effects. Among others, the collision rate is increased and, with it, the rate of momentum transfer from the moving walls into the bulk of the fluid-particle mixture; normal stress differences become larger and the particle-rich layer near the walls becomes denser. Comparable effects are found by increasing the particle density and the particle Reynolds number. The two normal stress differences are found to be both negative and comparable in spite of their very different physical origin. Additional results concern the wall slip, the stresslet, the effects of a nonzero collisional tangential force, the wall stress, and others. The great importance of particle-particle and particle-wall collisions reveals itself in influencing the rheology of the mixture, the normal stress differences, and the transport of momentum.

DOI: [10.1103/PhysRevFluids.5.084301](https://doi.org/10.1103/PhysRevFluids.5.084301)**I. INTRODUCTION**

The importance of particulate flows in nature and technology has motivated a rich literature devoted to improving our understanding of the physical processes that determine their behavior, an important aim being the development of reliable reduced-order models for their prediction. Particle-resolved simulations play an important role in this effort as they have the potential to facilitate an understanding of the detailed microphysics of these flows. Until fairly recently, the vast majority of these studies have been devoted to viscous suspensions at vanishing Reynolds number [see, e.g., Refs. 1–4]. Among others, an important result of these studies is the anisotropy of the pair distribution function which is at the root of the non-Newtonian behavior of suspensions manifesting itself in shear-thickening [5], nonzero normal stress differences [6], and shear-induced migration [1,7].

In the past few years improvements in algorithms and hardware have made particle-resolved numerical simulation possible at finite Reynolds numbers, first with the lattice-Boltzmann method

*gzhou4@jhu.edu

†aprosp@central.uh.edu

TABLE I. A representative list of papers devoted to the numerical study of fluid-particle mixtures in shear flow; ϕ is the particle volume fraction, ρ_p/ρ the ratio of the particle to the fluid density, Re_p and St the particle Reynolds and Stokes numbers defined in Eqs. (1) and (2), H/d the ratio of the gap width to the particle diameter, and N_{part} the number of particles in the simulation.

| Reference | ϕ , | ρ_p/ρ | Re_p | St | H/d | N_{part} |
|----------------------------|------------|---------------|----------|----------------|----------|-------------------------|
| Verberg and Koch [8] | 10–41 | 450–4500 | 0.04–40 | 10–100 | 12 | 64–240 |
| Kulkarni and Morris [9] | 5–30 | 1 | 0.04–20 | ~ 0 –1.67 | 10 | 77–516 |
| Yeo and Maxey [10] | 20–40 | – | 0 | – | 5–15 | 285–1718 |
| Yeo and Maxey [11] | 20, 30, 40 | 1 | 0.02–8 | ~ 0 –0.67 | ∞ | 438, 657, 876 |
| Haddadi and Morris [12] | 10–35 | 1 | 0.02–20 | ~ 0 –1.67 | 10 | ~ 191 – ~ 668 |
| Gallier <i>et al.</i> [13] | 10–55 | – | 0 | 0 | 10 | 1,000 |
| Fornari <i>et al.</i> [14] | 5–30 | 1 | 4–40 | 0.33–3.33 | 1.5–6 | – |
| Rahmani <i>et al.</i> [15] | 5–38 | 1 | 0.002–20 | ~ 0 –1.67 | 10 | ~ 95 – ~ 726 |
| Present | 5–33 | 2.5–10 | 20, 40 | 3.3–12.2 | 20 | 800–5000 |

[see, e.g., Refs. 8,16–18] and, more recently, with the immersed boundary method [see, e.g., Refs. 14,19–26] and others [see, e.g., Refs. 10,27,28]. A representative list, focused on the object of the present study, namely, shear flow, is given in Table I, which also shows the parameter range investigated in the various references. It can be seen from this table that all the studies, with the exception of Ref. [8], which was focused on gas-solid systems, have considered neutrally buoyant particles. This is of course the case of greatest relevance for experiments if gravitational settling is to be avoided. Nevertheless, an exploration of the effects of enhanced inertia associated with particles heavier than the fluid is also valuable to illuminate the physics of the particle-fluid interaction when the latter has a strong influence on the particle motion. It is the purpose of this paper to describe some results of resolved numerical simulations of this type. While our focus is on particles heavier than the suspending fluid, gravity is not considered.

Inertia is of particular significance in steady shear flow as, in its laminar single-phase counterpart, it plays no role. It will be shown that, as the particle density is made progressively larger, the resulting stronger memory of their earlier state of motion introduces significant effects. Among others, the collision rate is increased and, with it, the rate of momentum transfer from the moving walls into the bulk of the fluid-particle mixture is facilitated, normal stress differences become larger and the particle-rich layer near the walls becomes denser. Comparable effects are found by increasing the particle density and the particle Reynolds number. While, with increasing density, features such as the collision rate become close to the corresponding results for granular gases, subtle differences remain which have important consequences on wall and bulk shear stress and other features of the flow.

II. BRIEF DESCRIPTION OF THE SIMULATIONS

We consider a shear flow between two smooth parallel no-slip planes, separated by a distance H , moving along the x axis in opposite directions with velocities $\pm U$, so that the nominal shear rate is $\dot{\gamma} = 2U/H$ and the system Reynolds number $Re_s = 2HU/\nu$, with ν the fluid kinematic viscosity. The particle Reynolds number is defined by

$$Re_p = \frac{4a^2\dot{\gamma}}{\nu}, \quad (1)$$

with a the particle radius. We carried out simulations with $Re_p = 20$ and 40; the ratio $H/(2a) = 20$ was kept fixed so that $Re_s = 400 Re_p$. An important parameter characterizing the particle behavior

is the Stokes number, which we define by

$$\text{St} = \dot{\gamma} \tau_p = \frac{2U}{H} \left[\frac{2}{9} \frac{a^2}{\nu} \left(\frac{\rho_p}{\rho} + \frac{1}{2} \right) \right]. \quad (2)$$

Here ρ_p and ρ are the particle and fluid density, respectively, and the terms in brackets will be recongized as the time constant of inertial particles. The values of St quoted in Table I have been calculated using this relation and, therefore, in some cases they are different from those quoted in the original publications which often use the viscous particle time constant $\tau_p = 2\rho_p a^2 / (9\rho\nu)$. We mostly focus on the density ratio $\rho_p/\rho = 5$ presenting more limited results for $\rho_p/\rho = 2.5$ and 10. The computational domain extends over $80a$, $20a$, and $40a$, respectively, in the flow direction x , the spanwise direction y and the gradient direction z . Periodicity conditions are imposed in the x and y directions. With volume fractions $\phi = 5.2\%$, 21% , and 33% , this computational domain contains 800, 3200, and 5000 particles, respectively.

We have carried out particle-resolved simulation by means of the PHYSALIS method which is described in detail in a number of papers [see, e.g., Refs. 29–32]. The method is based on the observation that, due to the no-slip condition, near the particle the fluid motion differs little from rigid-body motion so that, in the particle rest frame, velocities are small, inertia is negligible, and the Stokes approximation is applicable. After a local change of frame to the particle rest frame, this circumstance makes the known Lamb general solution of Stokes equations locally applicable [33,34]. This solution is used as a “bridge” between the particle surface and the closest nodes of a regular Cartesian grid, which constitute an internal boundary for a finite-difference solution of the fully nonlinear Navier-Stokes equations. The local Lamb solution is in terms of unknown coefficients which are determined iteratively until the local Stokes analytical solution matches the Navier-Stokes solution. A useful feature of the method is that these coefficients are proportional to the force, couple, stresslet and higher-order multipoles associated with each particle, which therefore become available avoiding the need for data post-processing and additional computations. The Navier-Stokes equations are solved by a projection method on a staggered grid.

The collision model used in the simulations embodies a nonlinear Hertzian contact model which is activated whenever the distance between two particle centers becomes equal to a diameter. In addition to the normal force, colliding particles also interact via a tangential force \mathbf{F}_t which, for the sake of generality, we describe allowing properties of the colliding particles, α and β , including their radius, to be different [35]. The form of the tangential force is similar to that proposed in Ref. [36] and is given by

$$\mathbf{F}_t = k_t [\mathbf{w}_c - (\mathbf{w}_c \cdot \mathbf{n})\mathbf{n}] \Delta t, \quad (3)$$

with Δt the time step. The quantity in brackets is the tangential component of the relative velocity between the surfaces of the two particles at their point of contact and is given by

$$\mathbf{w}_c = \mathbf{w}_\alpha - \mathbf{w}_\beta - \frac{1}{2}(a_\alpha + a_\beta + h)(\Omega_\alpha - \Omega_\beta) \times \mathbf{n}. \quad (4)$$

Here \mathbf{w} and Ω are the particle velocity and angular velocity, \mathbf{n} is a unit vector directed along the line of centers and $a_\alpha + a_\beta + h$, with $h < 0$, is the distance between the particles’ centers. The stiffness k_t is given by Mindlin’s theory as [see, e.g., Ref. 37]

$$k_t = 8 \left(\frac{1 - \sigma_\alpha^2}{H_\alpha} + \frac{1 - \sigma_\beta^2}{H_\beta} \right)^{-1} \left(\frac{a_\alpha a_\beta}{a_\alpha + a_\beta} \right)^{1/2} (-h)^{1/2}, \quad (5)$$

in which $H = \frac{1}{2}E/(1 + \sigma)$ with E Young’s modulus and σ the Poisson ratio.

This collision model is complemented by a lubrication interaction which is activated when the distance between the particle surfaces is less than a radius. The same strategy is used for the particle-wall interactions; see Refs. [30,35] for details.

TABLE II. A concise view of the cases simulated in the present work; ϕ is the particle volume fraction averaged over the computational domain, $\text{Re}_p = 4a^2\dot{\gamma}/\nu$ is the particle Reynolds number, ρ_p/ρ is the ratio of the particle to fluid densities, St is the Stokes number, and N_p is the number of particles in the simulation.

| Case no. | Label | ϕ | Re_p | ρ_p/ρ | St | N_p |
|----------|--------------------|--------|---------------|---------------|-------------|-------|
| 1 | Reference | 21% | 20 | 5.0 | 6.1 | 3200 |
| 2 | High Re_p | 21% | 40 | 5.0 | 12.2 | 3200 |
| 3 | Small ϕ | 5% | 20 | 5.0 | 6.1 | 800 |
| 5 | Large ϕ | 33% | 20 | 5.0 | 6.1 | 5000 |
| 7 | Light | 21% | 20 | 2.5 | 3.3 | 3200 |
| 9 | Heavy | 21% | 20 | 10 | 11.7 | 3200 |

In this paper we describe the results of six simulations. To avoid repetition we will refer to them by the number shown in Table II. We use case 1 ($\phi = 21\%$, $\text{Re}_p = 20$, $\rho_p/\rho = 5$) as the reference case. Cases 2, 7, and 9 all have the same volume fraction but differ by having a larger Re_p and a smaller and larger density, respectively. Cases 3 and 5 differ by having, respectively, a smaller and a greater volume fraction. Table II also shows the Stokes number for the different cases. It may be noted that cases 2 and 9 have a very similar Stokes number. The former has a higher particle Reynolds number, 40, with $\rho_p/\rho = 5$, the latter has a smaller Reynolds number, 20, but a higher particle density $\rho_p/\rho = 10$. We will see that, for these two cases, many of the results that follow are very similar. This fact suggests that inertia, whether due to flow or particle density, has similar effects on many features of these flows.

III. PARTICLE VOLUME FRACTION

We begin by showing in Fig. 1 the results of our simulations for the local particle volume fraction. This quantity is calculated by dividing the computational domain into 320 layers parallel to the plates with a thickness of one computational cell, by calculating the volume internal to particles in each layer, and averaging over time.

Several authors have reported on the formation, near the solid walls, of particle layers with a density larger than that in the bulk [8,10,15]. The results for $\text{Re} = 20$, $\rho_p/\rho = 5$ and $\phi = 5\%$, 21%, and 33% (cases 3, 1, and 5) are shown in Fig. 1(a). Wall peaks are clearly visible for all cases. The peaks move toward the walls as the volume fraction is increased, consistent with Ref. [16], and a depletion layer adjacent to the wall is also clearly present at all volume fractions as found in Ref. [10]. However, unlike this latter work, the wall peaks do not grow relative to the bulk value as the volume fraction is increased. In fact, for $\phi = 33\%$, the bulk volume fraction is only slightly below the wall peak. Unlike ours, those simulations were conducted for $\text{Re}_p = 0$ and included only a model for lubrication interactions with the wall, but no actual collisions. The combination of a finite-Reynolds number and collisions may be expected to disrupt the wall layers especially since, with our model, the collision force upon particle-wall collisions can acquire a component directed away from the wall. A trend similar to that of Ref. [10] was reported in Ref. [9] in which, however, the volume fraction was based on the position of the particle centers rather than on the distribution of the actual particle volume. A similar procedure applied to our data produces much higher wall volume fractions than shown in the figure. It can be seen from Fig. 1(b), which shows the volume fraction for $\text{Re}_p = 20$ and $\phi = 21\%$ for different density ratios, that the peak height tends to slowly increase with ρ_p/ρ . The result of Ref. [15] for $\phi = 38\%$ exhibits a much stronger layering than ours for 33%, likely due to their channel height which was half of ours. The connection of a pronounced layering with a limited channel height has been explored and explained in Ref. [14].

The increasing peak height with increasing particle density is an effect of collisions. As shown in Sec. IV, the collision rate increases with ρ_p/ρ and, with a higher rate, particles have a greater probability of reaching the walls. Once there, they cannot be easily dislodged due to the fact that,

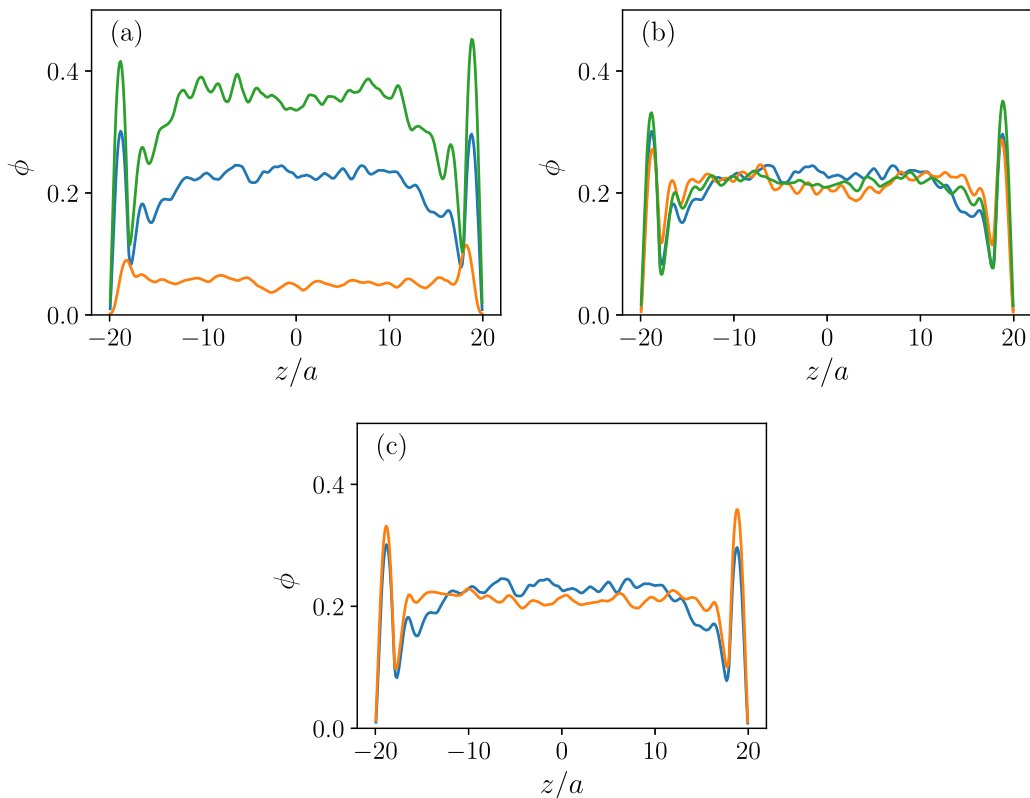


FIG. 1. Local time-averaged particle volume fraction between the plates. (a) Effect of the average volume fraction for $Re_p = 20$, $\rho_p/\rho = 5$ and, in ascending order, $\phi = 5\%$ (orange, case 3), 21% (blue, case 1), and 33% (green, case 5); (b) Effect of the particle density for $Re_p = 20$, $\phi = 21\%$ and in ascending order near the walls, $\rho_p/\rho = 2.5$ (orange, case 7), 5 (blue, case 1), and 10 (green, case 9); (c) Effect of the Reynolds number for $\phi = 21\%$, $\rho_p/\rho = 5$ and, in ascending order near the wall, $Re_p = 20$ (blue, case 1) and $Re_p = 40$ (orange, case 2).

in this region, collisions are strongly biased in the wall direction. This explanation is supported by Fig. 1(b), showing the effect of the density ratio for $Re_p = 20$ and $\phi = 20\%$, and by Fig. 1(c), showing the effect of the particle Reynolds number for $\rho_p/\rho = 5$ and the same volume fraction. While, in agreement with the results of Ref. [19], these two parameters do not exert a strong influence on the volume fraction in the bulk region of the flow, both figures indicate that the wall peak increases as both ρ_p/ρ and Re_p increase.

IV. COLLISIONS

Inertia has a significant effect on the particle collision rate which, in turn, influences several aspects of the flow under consideration as we have begun to see in the previous section.

Figure 2 and Table III show the collision rate (defined as the number of actual Hertzian contacts) per unit normalized time $\dot{\gamma}t$ as a function of normalized time for all the simulations described in this paper. The collisions of each particle are counted so that a binary collision, for example, would increase the collision count by 2. Thus, since, for this volume fraction, collisions involving more than two particles are rare, with a rate of 6400 collisions per unit time, approximately all the 3200 particles of the simulations with $\phi = 21\%$ on average would undergo a collision in a time unit, i.e., the time it takes for the plates to move one quarter of their length.

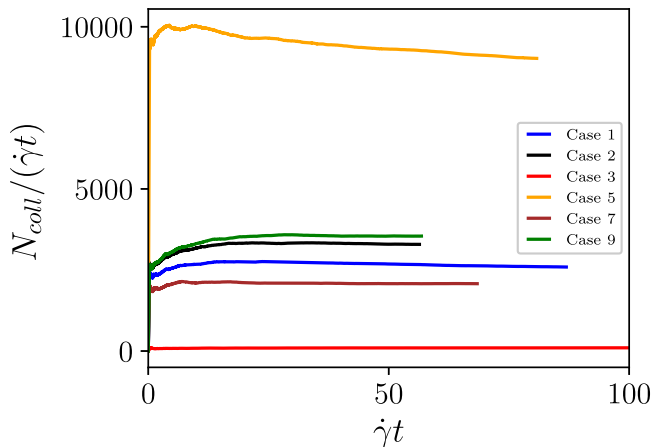


FIG. 2. Average normalized collision rate as a function of the dimensionless time for, in ascending order, $\text{Re}_p = 20$, $\phi = 5\%$, $\rho_p/\rho = 5$ (red, case 3); $\text{Re}_p = 20$, $\phi = 21\%$, $\rho_p/\rho = 2.5$ (brown, case 7); $\text{Re}_p = 20$, $\phi = 21\%$, $\rho_p/\rho = 5$ (blue, case 1); $\text{Re}_p = 40$, $\phi = 21\%$, $\rho_p/\rho = 5$ (black, case 2); $\text{Re}_p = 20$, $\phi = 21\%$, $\rho_p/\rho = 10$ (green, case 9); $\text{Re}_p = 20$, $\phi = 33\%$, $\rho_p/\rho = 5$ (orange, case 5).

Focusing on the results for $\text{Re}_p = 20$, $\phi = 21\%$ and, in increasing order, density ratios $\rho_p/\rho = 2.5$ (brown), 5 (blue), and 10 (green), we see that the corresponding collision rates are, approximately, 2100, 2600, and 3600 per unit time. The evident systematic increase with the density ratio is due to the increasing inertia that delays the particle response to the disturbance flow induced by the presence of a neighboring particle. This delayed response causes the first particle to continue in its original motion longer than it would have if it had a lower density and, in this way, it increases the collision rate. The same result was found in an earlier paper on a fluidized-bed-like system [38].

A different view of the collision rate f_c is given by Fig. 3 in which the rate is normalized as (Table III)

$$f_c^* = \frac{2af_c}{\sqrt{T}}, \quad (6)$$

with

$$T = \frac{1}{3} \langle \mathbf{u}'_p \cdot \mathbf{u}'_p \rangle, \quad (7)$$

TABLE III. Several numerical results of the present simulations; T^* is the granular temperature defined in Eq. (7) normalized by U^2 ; “coll” is the number of collision per unit normalized time $\dot{\gamma}t$; “norm coll” is the normalized collisions rate (6); “Couette dev’n” is the root-mean-squared deviation of the velocity profile from the Couette linear one (Sec. V and Fig. 6); “ang vel” is the normalized angular velocity in the vorticity direction Eq. (13).

| Case | $10^4 T^*$ | Coll | Norm coll f_c^* | Couette dev’n | Ang vel Ω_y^* |
|------|------------|-------|-------------------|---------------|----------------------|
| 1 | 2.72 | 2,617 | 4.96 | 0.11 | 0.58 |
| 2 | 4.95 | 3,314 | 4.65 | 0.07 | 0.62 |
| 3 | 25.3 | 102 | 0.25 | 0.02 | 0.77 |
| 5 | 3.20 | 9,054 | 10.1 | 0.17 | 0.51 |
| 7 | 2.31 | 2,078 | 4.27 | 0.12 | 0.58 |
| 9 | 5.20 | 3,545 | 4.86 | 0.07 | 0.63 |

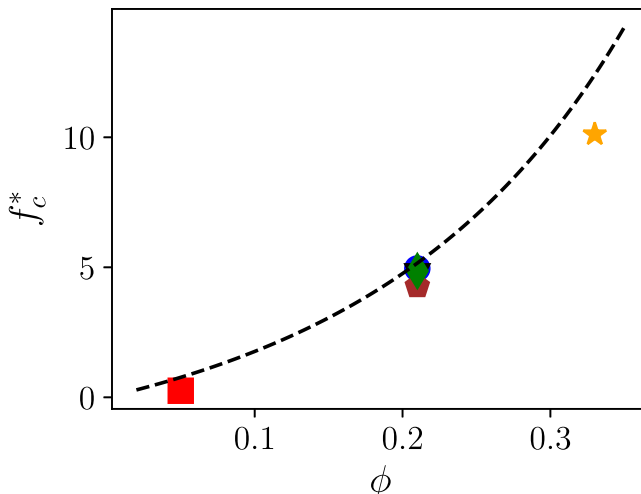


FIG. 3. Collision rate normalized according to Eq. (6), the collision rate in granular flow, shown by the dashed line. Circle: $Re_p = 20$, $\phi = 21\%$, $\rho_p/\rho = 5$ (case 1); triangle: $Re_p = 40$, $\phi = 21\%$, $\rho_p/\rho = 5$ (case 2); square: $Re_p = 20$, $\phi = 5\%$, $\rho_p/\rho = 5$ (case 3); star: $Re_p = 20$, $\phi = 33\%$, $\rho_p/\rho = 5$ (case 5); pentagon: $Re_p = 20$, $\phi = 21\%$, $\rho_p/\rho = 2.5$ (case 7); diamond: $Re_p = 20$, $\phi = 21\%$, $\rho_p/\rho = 10$ (case 9).

the granular temperature defined in terms of the mean particle velocity fluctuations, calculated as explained in Sec. V below; normalized values of this quantity are shown in Table III. The dashed line is the Enskog collision frequency for elastic hard spheres [see, e.g., Refs. 39,40],

$$f_E = 4g_2(\phi)d^2n\sqrt{\pi T}, \quad (8)$$

normalized in the same way; here $g_2(\phi)$ is the angle-averaged two-particle distribution function at contact, approximated by the Carnahan-Starling formula,

$$g_2(\phi) = \frac{1}{2} \frac{2 - \phi}{(1 - \phi)^3}. \quad (9)$$

It is remarkable that, except for the very dilute case with $\phi = 5\%$ and the dense case with $\phi = 33\%$, all the results fall very close to the Enskog collision frequency which, in principle, should only be applicable in the absence of interstitial fluid. Interstitial fluid has an obvious effect in slowing down the particles, but it also causes a particle to sense the approach of another particle. The first effect is probably strongest for the dilute case $\phi = 5\%$, in which the mean free path is longest and the effect of drag, therefore, largest. The second one may be more important at large volume fraction in which relative velocities are smaller and particles are more easily deflected. The normalized collision rates for the three density ratios $\rho_p/\rho = 2.5, 5$, and 10 are remarkably close to each other even though, as will be seen later, their effects on other flow quantities are significantly different. As far as collision rate is concerned, these cases with $\phi = 21\%$ seem to be close to a “sweet spot” which is least affected by the interstitial fluid.

V. VELOCITY FIELDS

Four examples of the horizontally averaged fluid and particle velocities in the direction of motion of the plates are shown in Fig. 4. Figures 4(a) and 4(b) are for $Re_p = 20$, $\rho_p/\rho = 5$, with $\phi = 21\%$ (case 1) and 33% (case 5), respectively; Figs. 4(c) and 4(d) are for $\phi = 21\%$, the former with $Re_p = 40$ and $\rho_p/\rho = 5$ (case 2), the latter with $Re_p = 20$ and $\rho_p/\rho = 10$ (case 9). The dashed line in these figures represents the single-phase Couette velocity profile. The two lines showing the phase

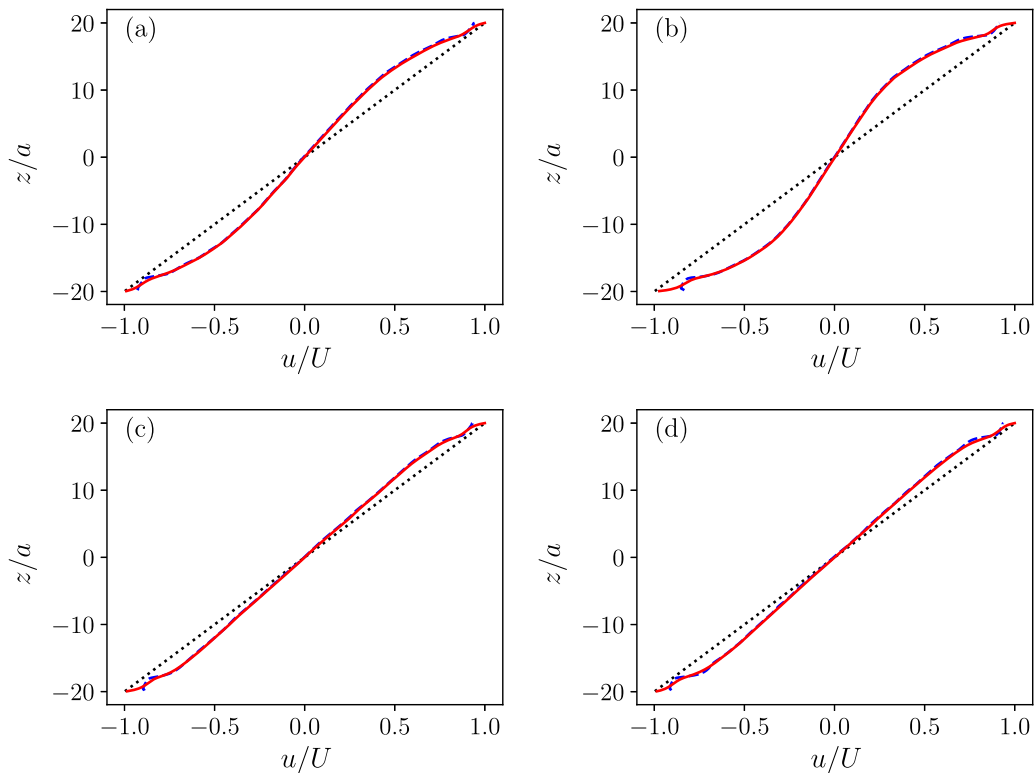


FIG. 4. Phase velocities normalized by the plate velocity U ; the dashed line shows the linear Couette velocity profile. (a) $Re_p = 20$, $\phi = 21\%$, $\rho_p/\rho = 5$ (case 1); (b) $Re_p = 20$, $\phi = 33\%$, $\rho_p/\rho = 5$ (case 5); (c) $Re_p = 40$, $\phi = 21\%$, $\rho_p/\rho = 5$ (case 2); (d) $Re_p = 20$, $\phi = 21\%$, $\rho_p/\rho = 10$ (case 9). The particle and fluid velocity are indistinguishable except very near the walls, an area enlarged in Fig. 7.

velocities essentially superpose except near the walls where particle slip becomes noticeable; we show detailed results on this region later. The formation of this “Vand layer” [41] is due to the fact that, due to excluded-volume effects, the volume fraction must decrease from about one particle diameter away from the wall until it vanishes at the wall itself (cf. Fig. 1). As the sketch of Fig. 5

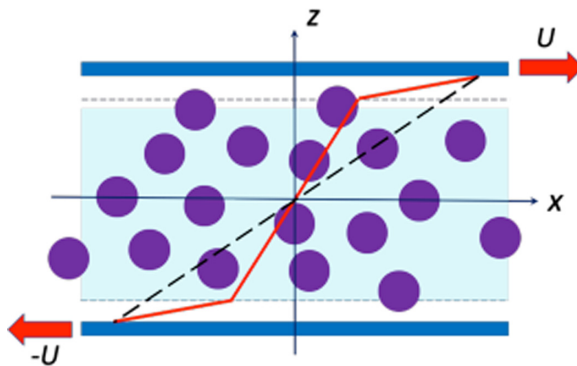


FIG. 5. Sketch of the velocity distribution in a system in which the effective viscosity near the walls is lower than in the bulk.

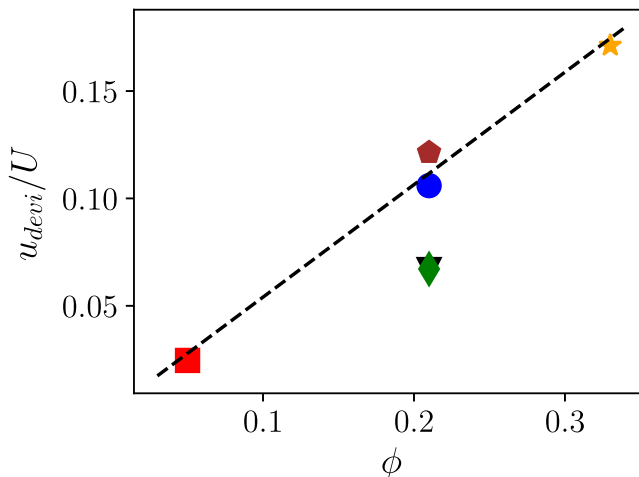


FIG. 6. Root-mean-square normalized difference u_{devi} between the mean fluid velocity and the velocity of the linear Couette profile at the same position for the cases considered in this study. Circle: $\text{Re}_p = 20$, $\phi = 21\%$, $\rho_p/\rho = 5$ (case 1); triangle: $\text{Re}_p = 40$, $\phi = 21\%$, $\rho_p/\rho = 5$ (case 2); square: $\text{Re}_p = 20$, $\phi = 5\%$, $\rho_p/\rho = 5$ (case 3); star: $\text{Re}_p = 20$, $\phi = 33\%$, $\rho_p/\rho = 5$ (case 5); pentagon: $\text{Re}_p = 20$, $\phi = 21\%$, $\rho_p/\rho = 2.5$ (case 7); diamond: $\text{Re}_p = 20$, $\phi = 21\%$, $\rho_p/\rho = 10$ (case 9).

shows, near-wall particles are therefore immersed in a medium with a lower (effective) viscosity than the bulk which cannot set them into motion as effectively. The result is a significant wall slip, visible in Fig. 4 and, in greater detail, in Fig. 7, and a smaller mean velocity gradient in the bulk of the system compared to the analogous single-phase flow.

The increased resistance to flow offered by the bulk as the volume fraction increases is evident in Figs. 4(a) and 4(b), in which the increased deviation from the single-phase profile is seen to increase as ϕ goes from 21% to 33%. Figures 4(c) and 4(d) show that increases of Re_p or of the particle density bring the velocity profiles closer to the linear Couette one, which implies a greater and greater ability of the system to transfer momentum in the cross-stream direction as inertia effects increase. In these latter two cases, the velocity profile is close to linear in the bulk of the flow approaching the velocity distribution sketched in Fig. 5. It will therefore be possible to define an effective viscosity for this region of the flow as will be done in Sec. VI. No clear definition of such a quantity is however possible for the other cases.

To illustrate the deviation of the profiles from the linear one we show in Fig. 6 the root-mean-square difference $u_{\text{devi}} = \sqrt{\langle (\langle u \rangle_{x,y,t} - \dot{\gamma}z)^2 \rangle_z}$ between the fluid velocity and the velocity of the linear profile at the same position for the three volume fractions considered in this study. Here the inner average is the average over time and planes parallel to the moving plates; the outer average is over the gap thickness. We can see here that the deviation increases with increasing ϕ and decreasing particle density reflecting the adverse influence of these opposite trends of the two variables on the transverse transport of momentum. This process occurs by the establishment of velocity gradients in the fluid and by the transverse motion of particles and their collisions, which are limited by increasing ϕ . Increasing the particle density, however, makes the collisions stronger and more frequent, which benefits the cross-stream momentum transport thus reducing the deviation from the linear profile. This interpretation is supported by the observation that the same effect is found by increasing the Reynolds number as shown by the near coincidence of the symbols with $\text{Re}_p = 20$, $\rho_p/\rho = 10$ (diamond), and $\text{Re}_p = 40$, $\rho_p/\rho = 5$ (downward triangle). A similar ability of increased inertia to promote cross-stream transfer is present in the heat-transfer results of Ref. [42] and (for momentum transfer only) it is visible in the results of Ref. [8], although a quantitative comparison is not possible due, first, to the order-of-magnitude difference of the fluid-to-particle density ratio and,

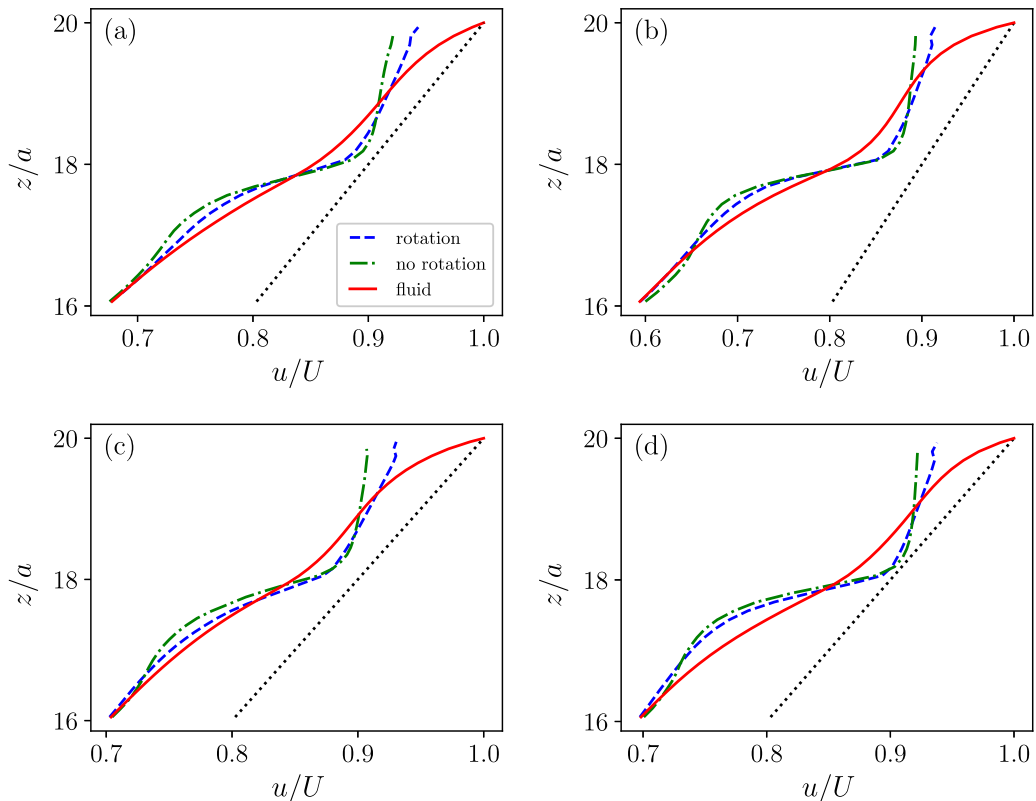


FIG. 7. Detail of phase velocities near the walls. The dotted line is the linear Couette velocity profile, the solid line is the fluid velocity, and the dashed and dash-dotted lines the particle material velocity including and excluding the particle rotation, respectively. (a) $Re_p = 20$, $\phi = 21\%$, $\rho_p/\rho = 5$ (case 1); (b) $Re_p = 20$, $\phi = 33\%$, $\rho_p/\rho = 5$ (case 5); (c) $Re_p = 40$, $\phi = 21\%$, $\rho_p/\rho = 5$ (case 2); (d) $Re_p = 20$, $\phi = 21\%$, $\rho_p/\rho = 10$ (case 9).

second, to the use by these authors of an artificially roughened wall to decrease the particle-wall slip.

Details of the phase velocities in the direction of the flow near the upper wall are shown for two cases in Fig. 7. Here the dotted line is the Couette profile and the solid line joining it at the top is the fluid velocity. Since the local particle volume fraction adjacent to the walls is small, the fluid velocity distribution in this region closely represents the entire mixture velocity as well. The particle velocity is represented in two ways. The dashed line is the velocity of the particle material in the flow direction. The dash-dotted line is obtained by attributing to each point in the particle the translational velocity of its center. The difference between the two results is due to particle rotation which will mostly be clockwise near the upper wall and therefore increase the velocity with respect to that of a pure translatory motion within one radius from the wall and decrease it in the region immediately below. One notices in Fig. 7(c) a somewhat larger slip velocity for the $Re_p = 40$ case and a somewhat larger difference between the two results for the particle phase velocity indicating a stronger effect of rotation. The effect of rotation in the other cases is very similar, which shows that rotation is essentially dictated by the plate motion with little if any effect of the particle density.

The four panels of Fig. 8 show the distribution of the particle velocity fluctuations \mathbf{u}'_p in the gap between the plates for the same four cases of Fig. 4. In these figures the rightmost group of points (blue) refers to the fluctuations in the streamwise direction and the others (green and yellow) to those in the orthogonal plane, which are seen to be very comparable. To generate these

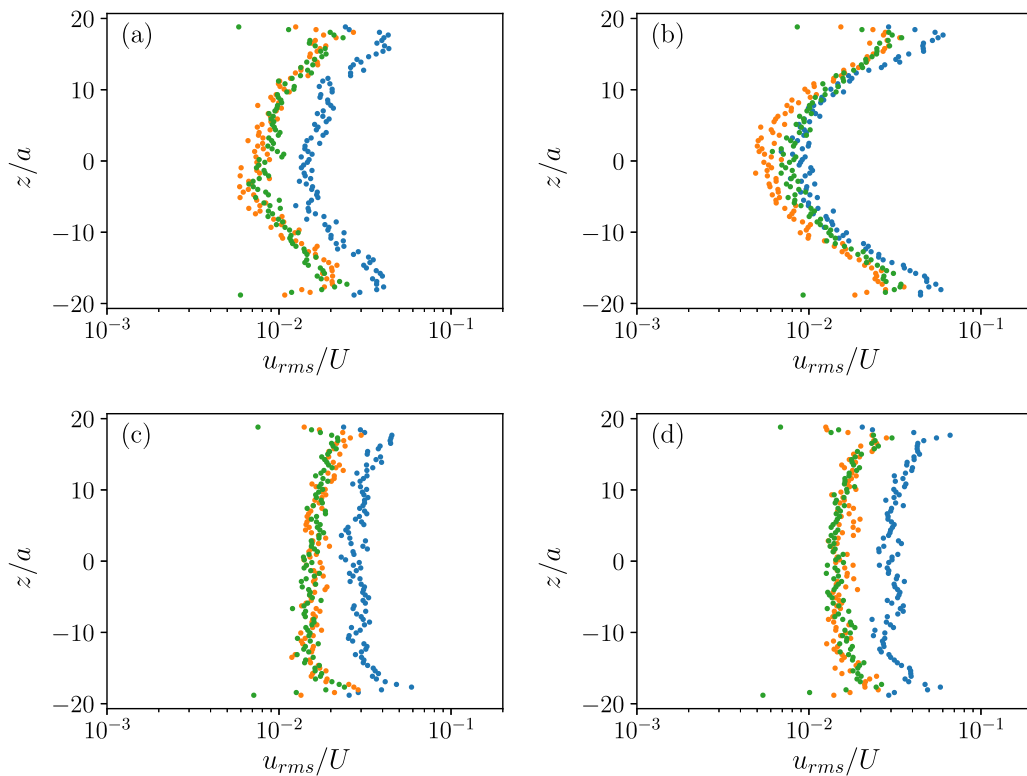


FIG. 8. Distribution of the normalized particle velocity fluctuations in the gap between the plates; the rightmost group of points (blue) are the fluctuations in the streamwise direction and the others (green and yellow) those in the orthogonal plane. (a) $\text{Re}_p = 20$, $\phi = 21\%$, $\rho_p/\rho = 5$ (case 1); (b) $\text{Re}_p = 20$, $\phi = 33\%$, $\rho_p/\rho = 5$ (case 5); (c) $\text{Re}_p = 40$, $\phi = 21\%$, $\rho_p/\rho = 5$ (case 2); (d) $\text{Re}_p = 20$, $\phi = 21\%$, $\rho_p/\rho = 10$ (case 9).

figures the computational domain was divided into 100 layers, each one with the thickness of three computational cells. Each point in the figure shows the root mean square velocity fluctuation averaged over all the particles in that layer.

For $\phi = 21\%$ and 33% , $\rho_p/\rho = 5$ and $\text{Re}_p = 20$ (cases 1 and 5), the fluctuations are large near the wall but decrease approaching the bulk, a tendency that increases with the volume fraction. This feature indicates the difficulty with which the wall momentum, which is the ultimate source of the fluctuations, is transported into the bulk that was already apparent in the deviation of the velocity distribution from the linear profile in Figs. 4(a) and 4(b) and in Fig. 6. If inertia is increased by increasing the Reynolds number, as in Fig. 8(c), or by increasing the particle density, as in Fig. 8(d), the velocity fluctuations become quite comparable throughout the gap. Increased inertia favors the transport of cross-stream momentum as already noticed in connection with the smaller deviation of the mean velocity distribution from the Couette profile in Fig. 6. A similar beneficial effect of increased inertia is visible in the granular temperature reported in Ref. [8]. In all cases, as reported in Ref. [15], the velocity fluctuations along the direction of the flow are larger than those in vorticity-shear plane.

Finally, we turn to the particle velocity correlation coefficient which, in the i direction, is defined by

$$R_i = \frac{\langle [u_{p,i}^\alpha(t + \tau) - \langle u_{p,i}^\alpha \rangle_{t, N_p}] [u_{p,i}^\alpha(t) - \langle u_{p,i}^\alpha \rangle_{t, N_p}] \rangle_{t, N_p}}{\langle [u_{p,i}^\alpha(t) - \langle u_{p,i}^\alpha \rangle_{t, N_p}]^2 \rangle_{t, N_p}}. \quad (10)$$

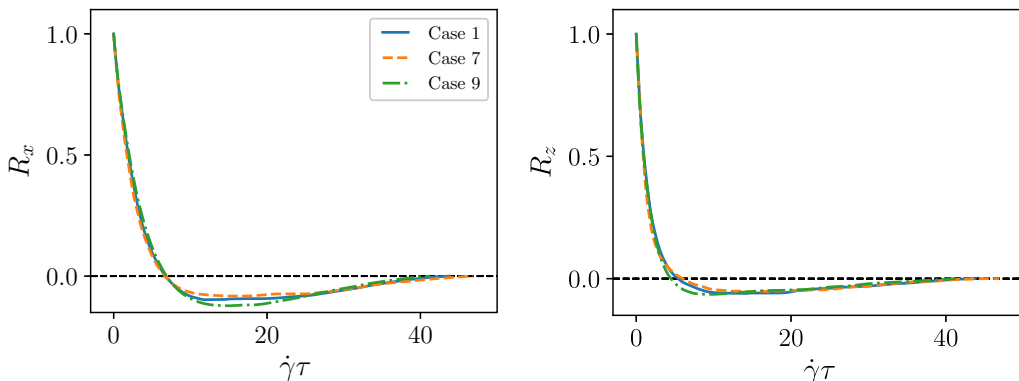


FIG. 9. Particle velocity correlation coefficient vs. the dimensionless delay time $\dot{\gamma}\tau$; the left panel is the correlation coefficient in the flow direction and the right panel that in the direction normal to the plates. Here $Re_p = 20$, $\phi = 21\%$, and $\rho_p/\rho = 2.5$ (orange, case 7), 5 (blue, case 1), and 10 (green, case 9).

Here, for brevity, we have used a synthetic notation. In more detail, $u_{p,i}^\alpha(t + \tau) = u_{p,i}^\alpha[\mathbf{y}^\alpha(t + \tau), t + \tau]$ is the i th component of the velocity of particle α at its instantaneous position $\mathbf{y}^\alpha(t + \tau)$, while $\langle u_{p,i}^\alpha \rangle_{t, N_p}$ is the particle velocity at the position z^α averaged over all the particles, over time and over x^α and y^α ; the subscript t denotes average over time and the subscript N_p average over the particles.

The correlation coefficient for $Re_p = 20$, $\phi = 21\%$ and $\rho_p/\rho = 2.5$ (orange, case 7), 5 (blue, case 1), and 10 (green, case 9) are shown in Figs. 9(a) and 9(b) in the direction x of the flow and in the direction z normal to the plates, respectively. In the range explored here, as found in Ref. [19], the particle density does not have a strong effect on the correlation coefficient. However, it is seen that larger inertia tends to increase the persistence of the correlation, as expected. Persistence of the velocity fluctuations in the flow direction x (left panel) and in the vorticity direction y (not shown) revert to zero slightly faster than persistence in the z direction (right panel). Another point of interest is that both correlation coefficients become negative before approaching zero. As noted in Ref. [43], this feature suggests that, on average, individual particles reverse their velocity with respect to the mean, which is expected in the case of binary collisions because of the very mechanics of the collision itself.

The two panels of Fig. 10 show, respectively, the effect of the volume fraction and of inertia on the velocity correlation. The coefficient becomes negative considerably later for the dilute case with $\phi = 5\%$, in which inertia maintains memory of the particle velocity for a long time before interaction with the other particles destroys it. For the same particle concentration, inertia, due to the Reynolds number or to particle density, does not seem to have a strong effect.

VI. STRESS

In considering the stress distribution in the gap it is useful to distinguish between the bulk and the wall regions. Starting from the former, we show in Fig. 11, as functions of time, the three distinct contributions to the (x, z) component of the stress due to the fluid velocity gradient, particle stress and collisions averaged over the flow domain with the exclusion of the two regions within three particle radii from the solid walls. The fluid velocity gradient is just the phase average of $\mu(\partial_x u_z + \partial_z u_x)$. The stresslet is defined by

$$s_{xz} = \frac{1}{2} \oint_s [z(\boldsymbol{\sigma} \cdot \mathbf{n})_x + x(\boldsymbol{\sigma} \cdot \mathbf{n})_z] ds, \quad (11)$$

in which $\boldsymbol{\sigma}$ is the total fluid stress and the integral is over the surface of the particle. One advantage of the PHYSALIS method is that the stresslet is generated directly by the simulation and does not

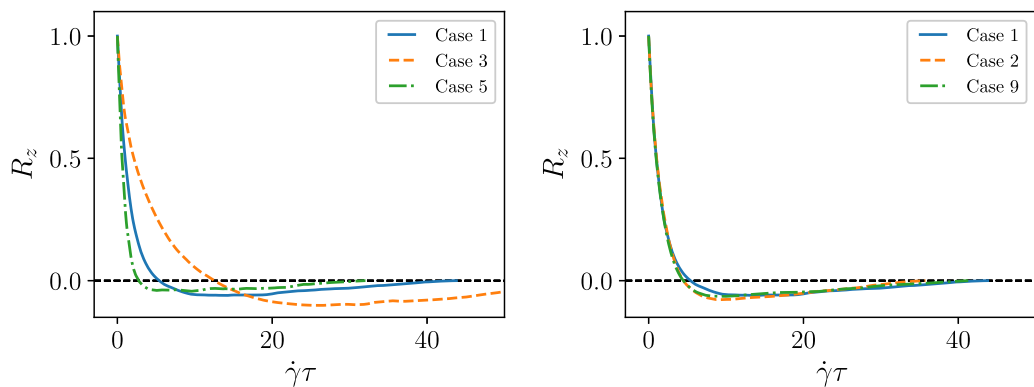


FIG. 10. Particle velocity correlation coefficient in the direction normal to the plates vs. the dimensionless delay time $\dot{\gamma}\tau$. The left panel highlights the effect of the average volume fraction for $\text{Re}_p = 20$ and $\rho_p/\rho = 5$; the lines are from left to right, for $\phi = 33\%$ (green, case 5), 21% (blue, case 1), and 5% (orange, case 3). The right panel shows the very weak effect of inertia for $\phi = 21\%$: $\text{Re}_p = 40$ $\rho_p/\rho = 5$ (orange, case 2), $\text{Re}_p = 20$ $\rho_p/\rho = 5$ (blue, case 1), and 10 (green, case 9).

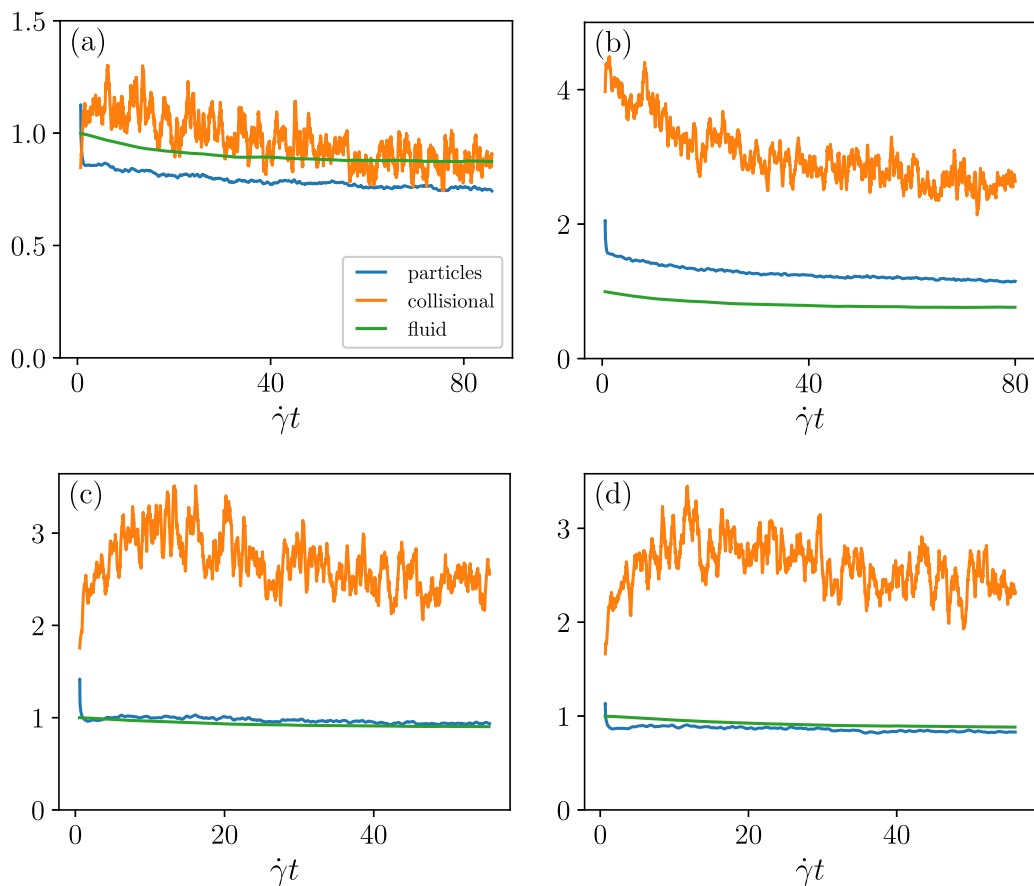


FIG. 11. Contributions to the bulk stress: fluid stress (green), particle stress Eq. (11) (blue) and collisional stress, Eq. (12) (orange). (a) $\text{Re}_p = 20$, $\phi = 21\%$, $\rho_p/\rho = 5$ (case 1); (b) $\text{Re}_p = 20$, $\phi = 33\%$, $\rho_p/\rho = 5$ (case 5); (c) $\text{Re}_p = 40$, $\phi = 21\%$, $\rho_p/\rho = 5$ (case 2); (d) $\text{Re}_p = 20$, $\phi = 21\%$, $\rho_p/\rho = 10$ (case 9).

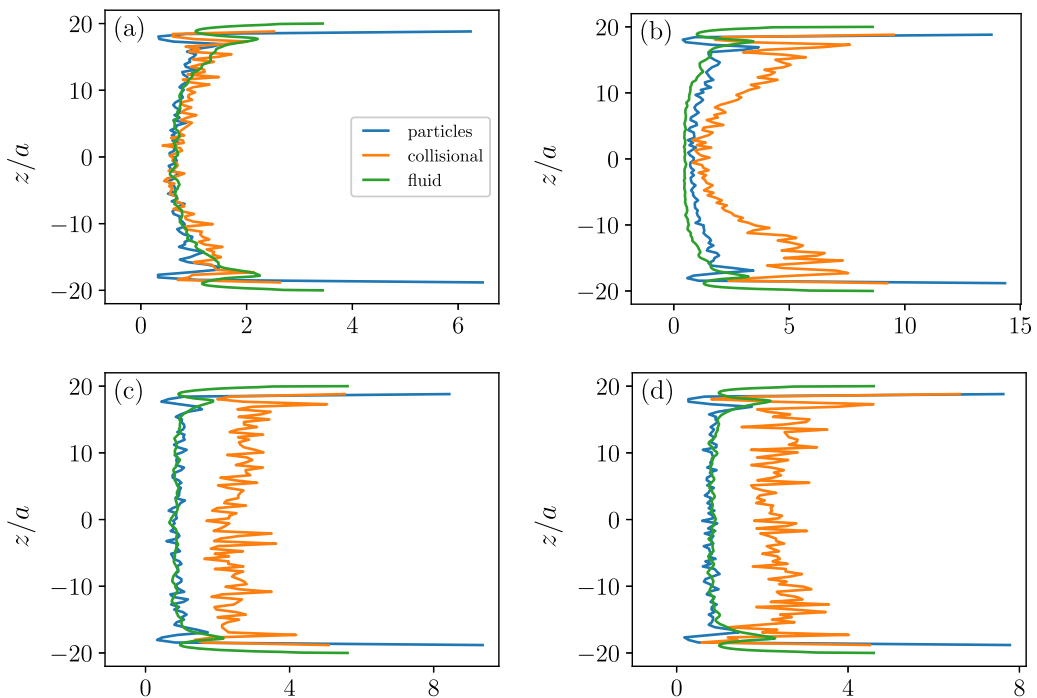


FIG. 12. Time-averaged distribution of the three contributions to the stress in the gap between the plates: fluid stress (green), particle stress (blue), and collisional stress (orange). (a) $\text{Re}_p = 20$, $\phi = 21\%$, $\rho_p/\rho = 5$ (case 1); (b) $\text{Re}_p = 20$, $\phi = 33\%$, $\rho_p/\rho = 5$ (case 5); (c) $\text{Re}_p = 40$, $\phi = 21\%$, $\rho_p/\rho = 5$ (case 2); (d) $\text{Re}_p = 20$, $\phi = 21\%$, $\rho_p/\rho = 10$ (case 9). The stress components are normalized by division by $\mu\dot{\gamma}$.

require the differentiation of the velocity field and its integration at the end of the time step as in the immersed-boundary method. The collisional stress is defined by

$$\hat{\sigma}_{xz}^c = \frac{1}{2}(zf_x^c + xf_z^c), \quad (12)$$

in which f_j^c is the sum of the collision and lubrication forces. Although f_j^c includes both forces, the lubrication component typically amounts at most to 10% of the total collision stress shown in the figures so that $\hat{\sigma}_{xz}^c$ essentially represents the effect of true collisions. It is shown in Ref. [44] that this break-up of the stress contributions is equivalent to that developed in the pioneering work of Ref. [45].

For $\text{Re}_p = 20$, $\phi = 21\%$ and $\rho_p/\rho = 5$ (case 1) the three contributions are comparable as can be seen in Fig. 11(a), but the collisional contribution is strongly dominant for $\phi = 33\%$ as reported in Ref. [9] (Fig. 11(b), case 5), as well as for the high-inertia cases $\text{Re}_p = 40$, $\rho_p/\rho = 5$ (Fig. 11(c), case 2) and $\text{Re}_p = 20$, $\rho_p/\rho = 10$ (Fig. 11(d), case 9). In the last three cases, the stresslet contribution exceeds that of the fluid stress. In viscous suspensions at zero Reynolds number contact interactions give a negligible contribution to the effective mixture viscosity at volume fractions below about 25–30% [46,47]. The difference with our results is yet another manifestation of the importance of inertia. All the contributions to the stress are larger near the beginning of the calculations. Their decrease slows down with time and appears to have nearly stabilized near the end of the simulations.

Figure 12 shows the distribution of the three contributions to the stress over the gap between the plates. In all cases the stresslet contribution is dominant near the plates (recall that the region included in the average stress contributions shown in Fig. 11 did not include three-radii-thick layers adjacent to the plates). The fluid contribution is the smallest, although it steeply increases near the wall as found in Ref. [15]. In Fig. 12(a), for $\text{Re}_p = 20$, $\phi = 21\%$, and $\rho_p/\rho = 5$ (case 1) all three

TABLE IV. The various contributions to the effective viscosity of the bulk region for cases 2 and 9 normalized by division by $\mu\dot{\gamma}$ and by division by $\mu\langle\partial_z u_{m,x}\rangle$. The sum of the fluid and stresslet contributions is close to 2, very similar to the predictions of both the Krieger and Eilers correlations for viscous suspensions at zero Re_p .

| Case | Normalized by $\mu\dot{\gamma}$ | | | | Normalized by $\mu\langle\partial_z u_{m,x}\rangle$ | | | |
|--|---------------------------------|-----------|------------|-------|---|-----------|------------|-------|
| | Fluid | Stresslet | Collisions | Total | Fluid | Stresslet | Collisions | Total |
| 2 ($\text{Re}_p = 40, \rho_p/\rho = 5$) | 0.84 | 0.90 | 2.51 | 4.33 | 1 | 1.05 | 2.94 | 5.00 |
| 9 ($\text{Re}_p = 20, \rho_p/\rho = 10$) | 0.84 | 0.81 | 2.41 | 4.11 | 1 | 0.96 | 2.85 | 4.81 |

contributions are comparable and similarly distributed in the gap. For the larger volume fraction $\phi = 33\%$ of Fig. 12(b) (case 5), the collisional stress near the wall is much larger, reflecting the particle distribution seen in Fig. 1(a) and the intense collisional activity responsible for the velocity fluctuations in Fig. 8(b). In the two higher inertia cases with $\text{Re}_p = 40$ of Fig. 12(c) (case 2) and $\rho_p/\rho = 10$ of panel (d) (case 9) the collisional component dominates, while the other two components are comparable; all three components are fairly uniformly distributed in the bulk in keeping with the very nearly linear velocity distribution visible in Figs. 4(c) and 4(d) and the approximately uniformly distributed velocity fluctuations for these cases shown in Figs. 8(c) and 8(d).

In these two latter cases the near uniformity of the three components permits us to define the corresponding contributions to the effective mixture viscosity relative to the fluid viscosity. This step can be taken in two ways, either by dividing the computed stress by $\mu\dot{\gamma}$, or by dividing it by $\mu\langle\partial_z u_{m,x}\rangle$, in which $u_{m,x}$ is the mixture velocity in the flow direction and the angle brackets indicate an average taken over time and the same bulk region used to generate the results of Fig. 11. In the first case one would be using the nominal shear rate which, however, is rather unrepresentative of the true shear rate in the gap as can be seen, e.g., in Fig. 4. For this reason, the second alternative seems preferable as it involves the actual velocity gradient rather than that estimated as in a Couette flow. Since, as can be seen, e.g., in Fig. 4, $\dot{\gamma} > \langle\partial_z u_{m,x}\rangle$, the second alternative also leads to larger values.

The results of the two alternatives are shown in Table IV. In both cases the collisional contribution accounts for more than 60% of the total. For the 21% volume fraction of both of these cases the well-known Eilers and Krieger [48] correlations predict a normalized effective viscosity of about 2 which is close to the sum of the fluid and stresslet effects but less than half the collisional contribution. Of course, collisions have a much stronger effect in the presence of significant inertia, a situation not considered in the development of these correlations.

Turning to the wall stress, we show in Fig. 13, versus time, the fluid and collisional stress on the walls normalized by division by $\mu\dot{\gamma}$. The collisional contribution was calculated by summing components of the collisional impulse in the flow direction over a certain interval of time and dividing by the time interval and the plate area. In all cases the collisional stress is comparable or even exceeds the fluid stress. The effect is particularly strong in the high-volume-fraction case of Fig. 13(b) and in the large-particle-density case of Fig. 13(d). In deducing an effective viscosity from these results one is faced with the same ambiguity as for the bulk effective viscosity, namely, whether to divide the stress by the second alternative also leads to larger values.

The results of both procedures are shown in Table V. One notices here a very large contribution from the fluid velocity gradient which, as indicated in Fig. 5 and, more quantitatively, in Fig. 7, is significantly larger than $\dot{\gamma}$. Reference [15] used the first normalization and, for $\text{Re}_p = 20$, $\phi = 20\%$ and $\rho_p/\rho = 1$, reported values of around 2.5, about 30% smaller than the fluid contribution that we calculate. The reasons for this discrepancy are unclear as the way in which the wall stress is calculated is not specified in the reference. Provisions for lubrication were not included; in addition, inertial effects would have been smaller since the particles had the same density as the fluid.

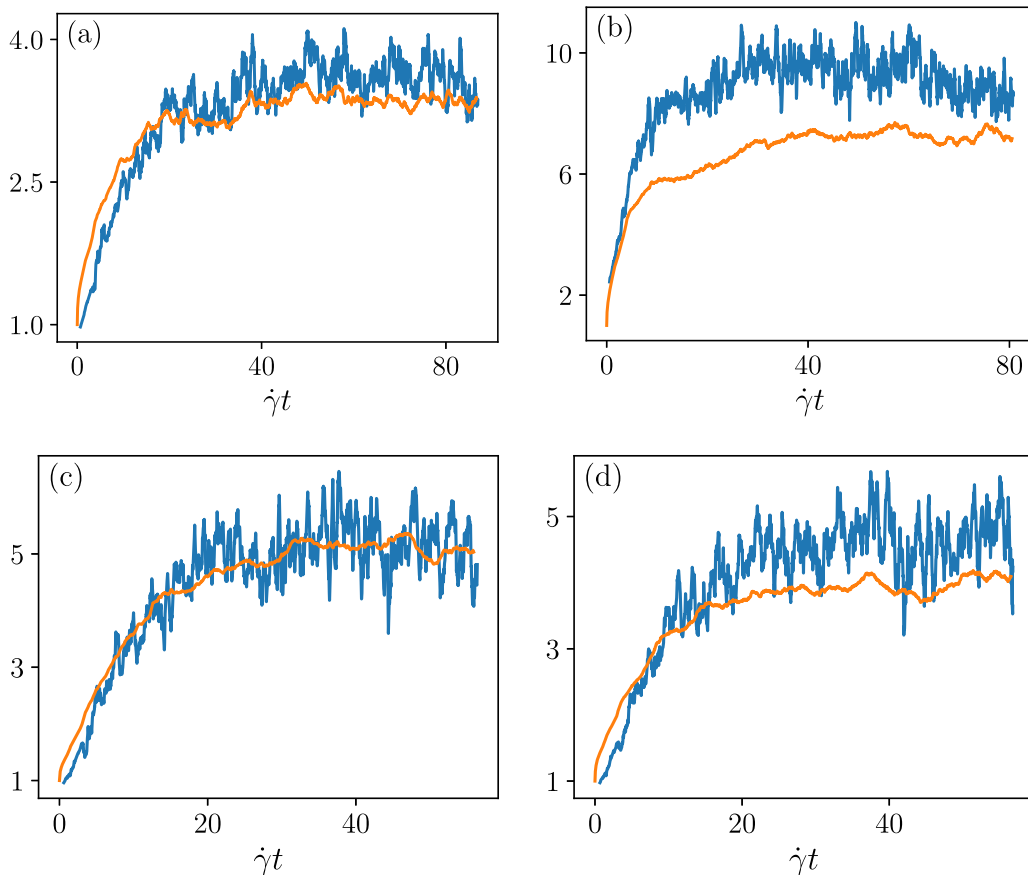


FIG. 13. Contributions to the wall stress from the fluid (orange) and particle-wall collisions (blue), nondimensionalized by division by $\mu\dot{\gamma}$, vs. nondimensional time $\dot{\gamma}t$. (a) $Re_p = 20$, $\phi = 21\%$, $\rho_p/\rho = 5$ (case 1); (b) $Re_p = 20$, $\phi = 33\%$, $\rho_p/\rho = 5$ (case 5); (c) $Re_p = 40$, $\phi = 21\%$, $\rho_p/\rho = 5$ (case 2); (d) $Re_p = 20$, $\phi = 21\%$, $\rho_p/\rho = 10$ (case 9).

Figure 14 permits a direct comparison among the fluid component of the wall stress for all the cases. Generally speaking, the fluid stress increases with volume fraction, inertia and the Reynolds number. Turning specifically to the effect of particle density, we do not notice much difference between $\rho_p/\rho = 2.5$ (brown) and 5 (blue), but the result for $\rho_p/\rho = 10$ (green) is clearly larger than for the other two cases. The fact that the stress appears to be slightly larger for $\rho_p/\rho = 2.5$ with

TABLE V. The various contributions to the effective viscosity of the wall region for cases 1, 2, 5 and 9 normalized by division by $\mu\dot{\gamma}$ and by division by $\mu\langle\partial_z u_{m,x}\rangle$.

| Case | Normalized by $\mu\dot{\gamma}$ | | | Normalized by $\mu\langle\partial_z u_{m,x}\rangle$ | | |
|------|---------------------------------|------------|-------|---|------------|-------|
| | Fluid | Collisions | Total | Fluid | Collisions | Total |
| 1 | 3.36 | 3.60 | 6.96 | 1 | 1.07 | 2.07 |
| 2 | 5.13 | 5.15 | 10.3 | 1 | 1.00 | 2.01 |
| 5 | 7.25 | 8.77 | 16.0 | 1 | 1.21 | 2.21 |
| 9 | 4.00 | 4.64 | 8.64 | 1 | 1.16 | 2.16 |

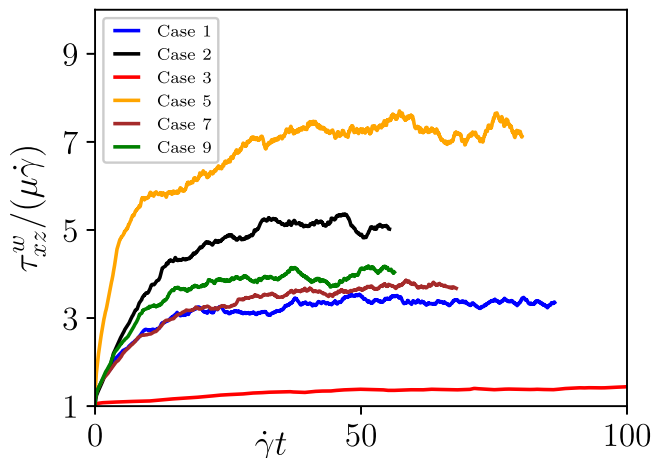


FIG. 14. Fluid contribution to the wall stress as a function of the nondimensional time $\dot{\gamma}t$. In ascending order the curves are for $\text{Re}_p = 20$, $\phi = 5\%$, $\rho_p/\rho = 5$ (red, case 3); $\text{Re}_p = 20$, $\phi = 21\%$, $\rho_p/\rho = 5$ (blue, case 1); $\text{Re}_p = 20$, $\phi = 21\%$, $\rho_p/\rho = 2.5$ (brown, case 7); $\text{Re}_p = 20$, $\phi = 21\%$, $\rho_p/\rho = 10$ (green, case 9); $\text{Re}_p = 40$, $\phi = 21\%$, $\rho_p/\rho = 5$ (black, case 2); $\text{Re}_p = 20$, $\phi = 33\%$, $\rho_p/\rho = 5$ (orange, case 5).

respect to $\rho_p/\rho = 5$, while both are smaller than the result for $\rho_p/\rho = 10$ opens the possibility of a nonmonotonic dependence of the wall fluid stress on the particle density, although the difference between the first two results is small and may also be due to imperfect statistical convergence.

VII. NORMAL STRESS DIFFERENCES

It is well known in the shear flow of low-Reynolds number suspensions that the particle pair distribution function is not isotropic, a feature which leads to nonzero-normal stress differences [6]. The results of Ref. [49] suggest that inertia contributes to this lack of isotropy and may be responsible for the shear-thickening of suspensions at finite Reynolds numbers. Our results also show a pronounced lack of isotropy in the present flow.

Figure 15 shows the projection of the pair distribution function on the plane of shear for the same cases shown in several earlier figures for our simulations. The scales are normalized by the particle diameter and the outer circle of the figure has a radius of 4 diameters. A significant density of pairs is clearly visible in the compression direction of the flow and a corresponding paucity in the extension direction. A plot of the higher volume fraction case versus distance from the test particle (not shown) reveals a double-peaked pair density distribution which is faintly visible as a more intensely colored outer ring also in Fig. 15(b). The two lower panels, corresponding to the larger inertia cases, exhibit a somewhat stronger anisotropy as compared with Fig. 15(a), as expected.

Since these figures are projections of the three-dimensional pair distribution function on the plane of shear, they do not give a clear picture of the pair distribution on the sides of the test sphere. This information is conveyed by Fig. 16, which shows the angular dependence of the pair distribution function at contact for $\text{Re}_p = 20$ and $\rho_p/\rho = 5$, the left panel with $\phi = 21\%$ (case 1) and the right panel with $\phi = 33\%$ (case 5). The data have been plotted assuming symmetry of the two sides of the test sphere with respect to its plane of symmetry parallel to the plane of shear. As already visible in the previous figure, contacts are virtually absent in the extension quadrants $0 < \theta < \frac{1}{2}\pi$ for $\varphi \sim 0$ (i.e., the upper half of sphere's front side) and $\frac{1}{2}\pi < \theta < \pi$ with $\varphi \sim \pi$ (i.e., the lower side of the sphere back), as is well known. Very few contacts are also seen in the range $\frac{1}{4}\pi < \theta < \frac{3}{4}\pi$ and its symmetric one on the other side of the sphere, namely, on the two lateral quarters of the sphere. This feature is likely a consequence of the fact that the centers of two spheres colliding in these regions

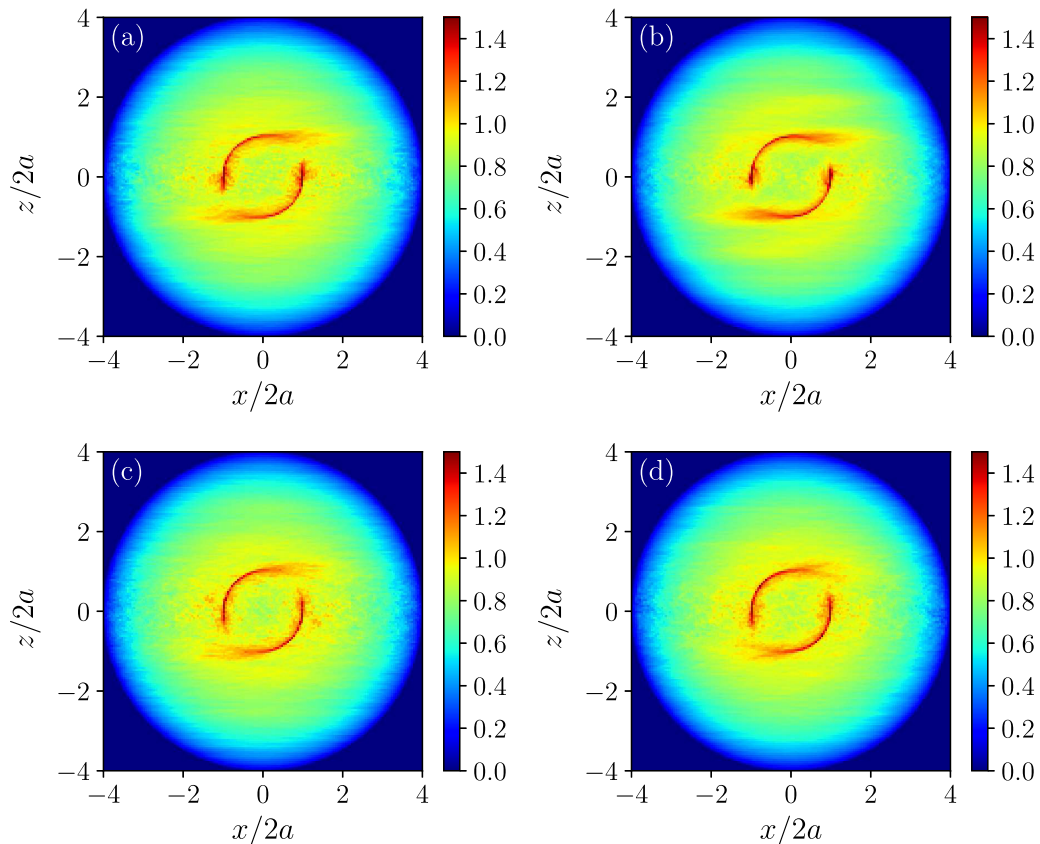


FIG. 15. Projection on the plane of shear of the pair distribution function in the neighborhood of the test particle. (a) $\text{Re}_p = 20$, $\phi = 21\%$, $\rho_p/\rho = 5$ (case 1); (b) $\text{Re}_p = 20$, $\phi = 33\%$, $\rho_p/\rho = 5$ (case 5); (c) $\text{Re}_p = 40$, $\phi = 21\%$, $\rho_p/\rho = 5$ (case 2); (d) $\text{Re}_p = 20$, $\phi = 21\%$, $\rho_p/\rho = 10$ (case 9).

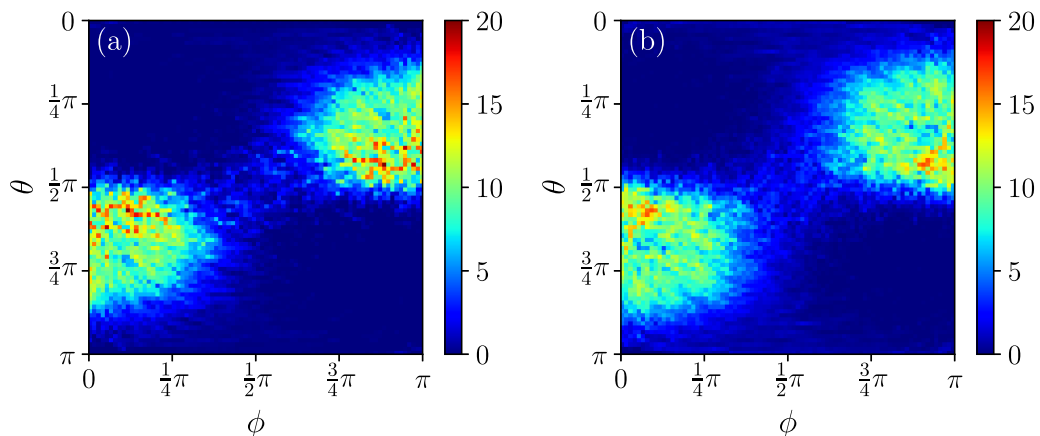


FIG. 16. Examples of the angular dependence of the pair distribution function at contact. Both figures are for $\text{Re}_p = 20$ and $\rho_p/\rho = 5$, in (a) for $\phi = 21\%$ (case 1) and in (b) for $\phi = 33\%$ (case 5).

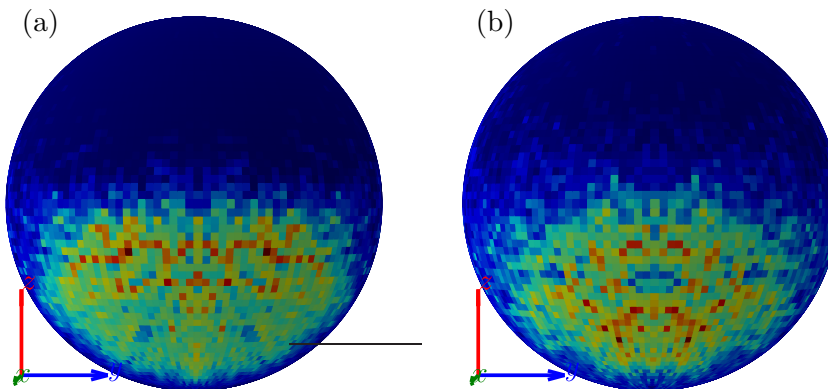


FIG. 17. Frontal three-dimensional view of the pair distribution function on contact with the test particle. The pixels are colored according to the frequency of contacts. The test particle moves out of the page, the gradient direction is up and the vorticity direction horizontally to the right. Both images are for $\text{Re}_p = 20$ and $\phi = 21\%$: (a) $\rho_p/\rho = 5$ (case 1); (b) $\rho_p/\rho = 10$ (case 9). A similar picture is found on the back of the sphere with the contacts occurring in the upper hemisphere.

would have a relatively small separation in z and, therefore, a smaller relative velocity that makes it easier for them to be deflected away from each other. The main difference between the two cases is a somewhat greater number of contacts in the denser one as expected.

A different view of the pair distribution function with focus on contact is afforded by Fig. 17, which shows a three-dimensional frontal view of the test particle for two cases with $\text{Re}_p = 20$ and $\phi = 21\%$, the reference case with $\rho_p/\rho = 5$ (left panel, case 1) and the high-density case with $\rho_p/\rho = 10$ (case 9). Here pixels are colored according to the frequency of contacts with other particles. The flow is out of the page, the gradient direction is up and the vorticity direction horizontally to the right. A similar picture is found on the back of the test sphere with the contacts occurring on the upper hemisphere. It is clear upon comparison that the region where contacts occur is somewhat smaller in the higher-density case since more massive particles are less susceptible to being deflected by the flow upon approaching another particle.

In suspension mechanics, the anisotropy of the pair distribution function is associated with nonzero normal stress differences $N_1 = \Sigma_{xx} - \Sigma_{zz}$ and $N_2 = \Sigma_{zz} - \Sigma_{yy}$, and the same is true in the present case. This is a long-standing issue in suspension mechanics as discussed in many papers [see, e.g., Refs. 1,6,12,47,50–52]. It is an established fact that N_2 is negative [see, e.g., Refs. 47,50], but the sign of N_1 is still uncertain as experiments are difficult and it is not clear to what extent the results may be affected by the rheometer walls [see, e.g., Refs. 10,13,52]. Numerical simulations mostly agree on a negative sign for N_1 , starting with the work of Ref. [6], including a series of later studies mentioned in the referenced review papers, until the recent study of Ref. [52].

Our results for these quantities are shown in Table VI where they are broken up into the contributions from the particle-particle interaction (including collision and lubrication) and from the stresslet; since the suspending fluid is Newtonian it gives no contribution to these quantities. These results have been obtained by calculating the average values of the collisional and stresslet contributions of each particle to the stress in the bulk of the suspension, namely, including only particles the center of which is at least three radii away from the walls, and normalizing by division by $\mu\dot{\gamma}$. We found that the collisional results were influenced by outlier values of the collisional contribution. This finding suggests that quantitatively correct contributions of this component would require much longer integration times than we could carry out. For this reason, in calculating the results shown in the table, after gathering the contributions of all the particles at each time step, we have dropped 1% of the largest and smallest values.

TABLE VI. Stresslet contribution, collisional contribution, and total normal stress differences normalized by $\mu\dot{\gamma}$.

| Case | Stresslet | | Collision | | Total | |
|------|-----------|-------|-----------|-------|-------|-------|
| | N_1 | N_2 | N_1 | N_2 | N_1 | N_2 |
| 1 | -0.43 | 0.14 | 0.06 | -0.31 | -0.37 | -0.17 |
| 2 | -0.63 | 0.16 | -0.08 | -0.54 | -0.71 | -0.38 |
| 3 | -0.13 | 0.02 | 0.00 | -0.01 | -0.13 | 0.01 |
| 5 | -0.57 | 0.18 | -0.16 | -0.78 | -0.73 | -0.60 |
| 7 | -0.42 | 0.15 | 0.06 | -0.29 | -0.36 | -0.14 |
| 9 | -0.48 | 0.11 | -0.09 | -0.41 | -0.57 | -0.30 |

One observes that both normal stress differences are negative and of comparable magnitude, as found in the inertialess simulations of Ref. [6], both becoming more negative as the particle volume fraction is increased. Comparison of the results for $\text{Re}_p = 20$ and 40 reveals an increase by about a factor of 2 for both N_1 and N_2 . Table VI shows that the largest contribution to N_1 comes from the stresslet, while the largest contribution to N_2 is due to particle-particle interaction. This finding is in agreement with the results of the authors of Ref. [46], who found that N_1 is mostly of hydrodynamic origin, whereas N_2 is mostly the result of contact interactions due to the fact that collisions occur predominantly in the plane of shear. The collisional contribution to N_1 is mostly small and changes sign, probably as a consequence of insufficiently converged statistics.

The second normal stress difference N_2 does not change appreciably as the particle density is increased from 2.5 to 5, but nearly doubles upon a further increase to 10. The effect appears dominated by collisions as the stresslet contribution is seen to be essentially insensitive to particle mass in the range we have explored. Both N_1 and N_2 are in modulus about an order of magnitude less than τ_{xz} as found in Ref. [6] for viscous suspensions.

VIII. EFFECT OF THE TANGENTIAL COLLISION FORCE

Recent work [see, e.g., Refs. 53–55] has shown the importance of particle-particle tangential contact forces in several phenomena exhibited by dense suspensions such as solidification during sudden impact and discontinuous, order-of-magnitude increases of the effective viscosity in the presence of intense shear. Although no such dramatic effects can be expected at the volume fractions considered in this study, these observations prompted us to repeat the simulation for case 1 ($\phi = 21\%$, $\rho_p/\rho = 5$, $\text{Re}_p = 20$) setting the tangential component Eq. (3) of the collision force to zero. We found that, while the collision rate is indistinguishable from that shown in Fig. 2, several significant aspects of the flow are affected.

Figure 18 compares the local, time-averaged volume fraction in the gap between the plates. Here the blue line is the previous result with a nonzero tangential contact force already shown in Fig. 1. Away from the walls the distributions coincide, but one notices a smaller secondary peak (balanced by a larger wall peak) with tangential dissipation. The average distribution of the particle material velocity is compared for the two cases in Fig. 19 (it will be recalled that the fluid velocity is indistinguishable except very near the walls). It is seen here that, as the tangential contact force is eliminated, the velocity distribution becomes closer to the linear Couette profile (dotted line). Both results indicate that the cross-stream momentum transfer is increased by the absence of tangential dissipation, as could have been anticipated. We have also calculated the effect of the tangential collision force on the second normal stress difference N_2 finding a (normalized) value close to -0.45 , to be compared with -0.31 as reported in Table VI.

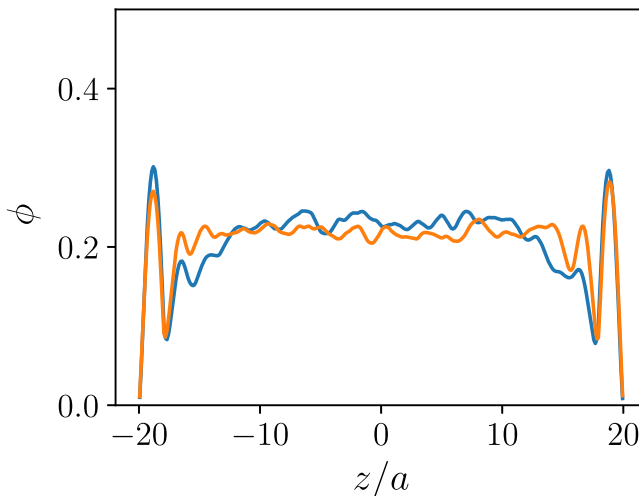


FIG. 18. Local time-averaged particle volume fraction between the plates for the reference case with $\phi = 21\%$, $\rho_p/\rho = 5$, $\text{Re}_p = 20$. Orange: zero tangential collision force; blue: nonzero tangential collision force; the latter results are the same as in Fig. 1.

Even on the basis of these very limited results we may conclude that the effects of the tangential collision force are profound and do not manifest themselves only in the dense case but affect suspension mechanics over nearly the entire volume fraction range.

IX. PARTICLE ROTATION

Figure 20 shows, for all the cases, $\langle \Omega_y^* \rangle$, the mean particle angular velocity in the vorticity direction, normalized by one half of the single-phase fluid vorticity $2U/H$:

$$\Omega_y^* = \frac{\Omega_y}{U/H}; \quad (13)$$

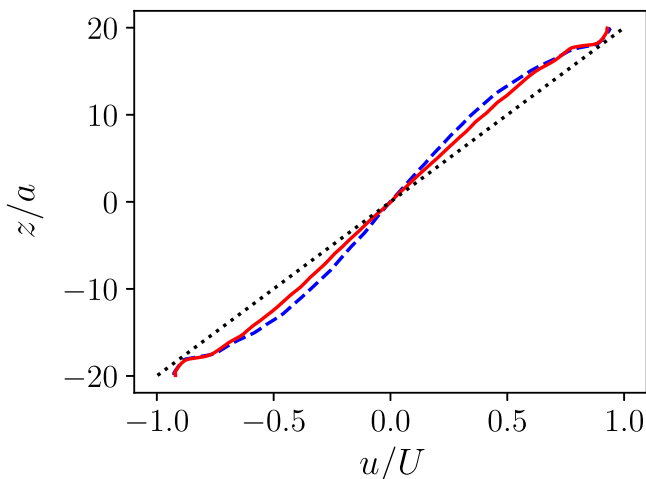


FIG. 19. Time-averaged particle phase velocity normalized by the plate velocity U with (dashed) and without (solid) a tangential component of the collision force; the dotted line shows the linear Couette velocity profile. Here $\text{Re}_p = 20$, $\phi = 21\%$, $\rho_p/\rho = 5$. The fluid velocity is nearly coincident with that of the particle phase except very near the walls (see Fig. 7).

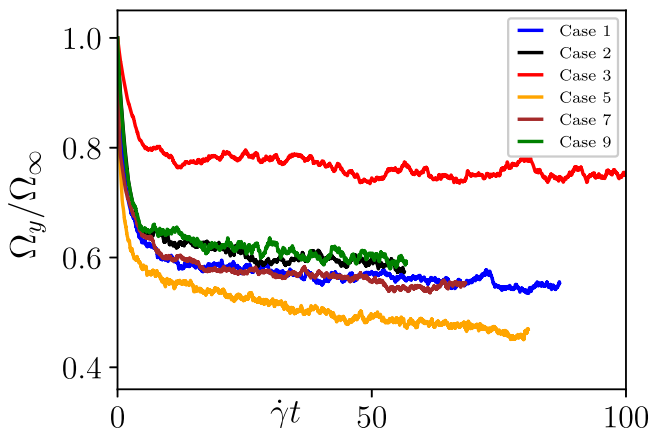


FIG. 20. Normalized particle angular velocity Ω_y^* defined in Eq. (13) vs. normalized time $\dot{\gamma}t$. In descending order the curves are for $\text{Re}_p = 20$, $\phi = 5\%$, $\rho_p/\rho = 5$ (red, case 3); $\text{Re}_p = 20$, $\phi = 21\%$, $\rho_p/\rho = 10$ (green, case 9); $\text{Re}_p = 40$, $\phi = 21\%$, $\rho_p/\rho = 5$ (black, case 2); $\text{Re}_p = 20$, $\phi = 21\%$, $\rho_p/\rho = 5$ (blue, case 1); $\text{Re}_p = 20$, $\phi = 21\%$, $\rho_p/\rho = 2.5$ (brown, case 7); $\text{Re}_p = 20$, $\phi = 33\%$, $\rho_p/\rho = 5$ (orange, case 5).

numerical values are provided in Table III. The simulations were initiated assigning to each particle the angular velocity $\mathbf{\Omega}_* = (0, 1, 0)$ in the three coordinate directions. It has been argued that the average particle angular velocity of an isotropic suspension at vanishing Reynolds number is the same as for an isolated particle in the same shear flow at any concentration [56]. The results of Ref. [56] at zero Reynolds number are in fair agreement with this prediction although the mean absolute value appears to increase somewhat as the volume fraction increases. The results of Ref. [12] at $\text{Re} = 0.05, 0.6$ and 1 show a similar 10–20% increase as the volume fraction goes from 10% to 30%. At first sight, our results seem to be very different, but it should be kept in mind that, as is evident from Figs. 4 and 7, the shear rate in our gap is rather far from the nominal shear rate $2U/H$ and it is non-uniform. If we try to characterize the mixture shear rate by the velocity gradient on the midplane, then we find that our calculated mean angular velocity is within 20% of half of this velocity gradient. The difference can be imputed to the nonuniformity of the mixture (cf. Fig. 1) and of the strain rate, in addition, of course, to inertial effects.

Since, as can be seen from Fig. 11, the mixture velocity gradient slowly decreases with time, so does the average particle rotation rate. The results for case 5 (orange line) suggest that true steady conditions may not have quite been reached by the end of the simulations for this case, probably due to the fact that it has the largest volume fraction, $\phi = 33\%$. A similar slow residual slow decline is also visible in the collision rate shown in Fig. 2. However, other quantities related to this case, such as the bulk and wall stresses in Figs. 11(b), 13(b), and 14 seem to be well converged. To a much lesser extent, a similar comment may be applicable to case 1 (blue line).

Comparison of Figs. 4(a) and 4(b) shows that the shear rate decreases with increasing volume fraction and, correspondingly, we see in Fig. 20 a decreasing angular velocity with increasing ϕ . Turning to the effect of particle density and Reynolds number, we see in Figs. 4(c) and 4(d) comparable shear rates and the corresponding particle angular velocities are also quite comparable.

X. SUMMARY AND CONCLUSIONS

In this paper we have described results of resolved simulations of a particle-fluid mixture with particle volume fraction in the range between 5% and 33% occupying the space between two parallel plates moving with equal velocities in opposite directions. Unlike other papers on this subject, summarized in Table I, we have considered particles heavier than the fluid, with a density ratio between 2.5 and 10, and two single-particle Reynolds numbers, 20 and 40. In this way we have

been able to focus on the effect of inertia finding that this property exerts a profound influence on many aspects of the flow including the distribution of particles and velocity in the gap between the plates, the collision rate, the stress and others.

The nonuniformity of the two-particle distribution function found in low-Reynolds-number simulations [5] is confirmed for our parameter range and results in significant normal-stress differences N_1 and N_2 . These quantities are both negative and of comparable magnitude, although they have different origin, the first one mostly determined by the flow and the second one strongly dependent on collisions [46]. Motivated by recent work on jamming [see, e.g., Refs. 53–55] we have conducted limited simulations in which the tangential component of the collision force was set to zero. We have found that this version of the model leads to significantly different particle and velocity distributions in the gap compared with the model with a nonzero tangential collisional force in spite of the relatively small particle volume fraction considered. Since the second normal stress difference is mostly determined by collisions, there is a strong effect on N_2 as well.

It is hoped that the gradual accumulation of results such as the ones reported here will help achieve a deeper understanding of particle-fluid systems beyond the low-Reynolds-number conditions that have mostly been studied so far. One positive outcome of these efforts would be the formulation of reduced-order models more realistic and mathematically well-posed than many that have been proposed. A serious problem on this path, however, is that of averaging. Our simulations have up to 5000 particles but, in spite of this relatively large number, the results still exhibit strong fluctuations that would prevent, for instance, the calculation of smooth time and space derivatives. Yet, it is essential to be able to calculate differential quantities of this type if the objective is the formulation of reduced-order models expressed in terms of differential equations. Statistical convergence cannot be achieved in situations of this type, which renders necessary the development of filtering methods capable to smoothen out the fluctuations present in the simulations. In an earlier paper we have shown how the use of a truncated Fourier series can achieve this result in a special case [38]. The development of a method of general applicability, however, still belongs to the future.

ACKNOWLEDGMENT

The numerical computations were carried out on the Sabine cluster of the University of Houston Research Computing Data Core.

-
- [1] M. M. Denn and J. F. Morris, Rheology of non-Brownian suspensions, *Annu. Rev. Chem. Biomol. Eng.* **5**, 203 (2014).
 - [2] E. Guazzelli and J. F. Morris, *A Physical Introduction to Suspension Dynamics* (Cambridge University Press, Cambridge, UK, 2012).
 - [3] M. Maxey, Simulation methods for particulate flows and concentrated suspensions, *Annu. Rev. Fluid Mech.* **49**, 171 (2017).
 - [4] J. J. Stickel and R. L. Powell, Fluid mechanics and rheology of dense suspensions, *Annu. Rev. Fluid Mech.* **37**, 129 (2005).
 - [5] J. F. Brady and J. F. Morris, Microstructure of strongly sheared suspensions and its impact on rheology and diffusion, *J. Fluid Mech.* **348**, 103 (1997).
 - [6] A. Sierou and J. F. Brady, Rheology and microstructure in concentrated noncolloidal suspensions, *J. Rheol.* **46**, 1031 (2002).
 - [7] F. Gadala-Maria and A. Acrivos, Shear-induced structure in a concentrated suspension of solid spheres, *J. Rheol.* **24**, 799 (1980).
 - [8] R. Verberg and D. L. Koch, Rheology of particle suspensions with low to moderate fluid inertia at finite particle inertia, *Phys. Fluids* **18**, 083303 (2006).

- [9] P. M. Kulkarni and J. F. Morris, Suspension properties at finite Reynolds number from simulated shear flow, *Phys. Fluids* **20**, 040602 (2008).
- [10] K. Yeo and M. R. Maxey, Dynamics of concentrated suspensions of non-colloidal particles in Couette flow, *J. Fluid Mech.* **649**, 205 (2010).
- [11] K. Yeo and M. R. Maxey, Dynamics and rheology of concentrated, finite-Reynolds-number suspensions in a homogeneous shear flow, *Phys. Fluids* **25**, 053303 (2013).
- [12] H. Haddadi and J. F. Morris, Microstructure and rheology of finite inertia neutrally buoyant suspensions, *J. Fluid Mech.* **749**, 431 (2014).
- [13] S. Gallier, E. Lemaire, L. Lobry, and F. Peters, Effect of confinement in wall-bounded non-colloidal suspensions, *J. Fluid Mech.* **799**, 100 (2016).
- [14] W. Fornari, L. Brandt, P. Chaudhuri, C. U. Lopez, D. Mitra, and F. Picano, Rheology of Confined Non-Brownian Suspensions, *Phys. Rev. Lett.* **116**, 018301 (2016).
- [15] M. Rahmani, A. Hammouti, and A. Wachs, Momentum balance and stresses in a suspension of spherical particles in a plane Couette flow, *Phys. Fluids* **30**, 043301 (2018).
- [16] J. Kromkamp, D. van den Ende, D. Kandhai, R. van der Sman, and R. Boom, Lattice Boltzmann simulation of 2D and 3D non-Brownian suspensions in Couette flow, *Chem. Eng. Sci.* **61**, 858 (2006).
- [17] A. J. C. Ladd and R. Verberg, Lattice-Boltzmann simulations of particle-fluid suspensions, *J. Stat. Phys.* **104**, 1191 (2001).
- [18] X. Yin and D. L. Koch, Hindered settling velocity and microstructure in suspensions of solid spheres with moderate Reynolds numbers, *Phys. Fluids* **19**, 093302 (2007).
- [19] W. Fornari, A. Formenti, F. Picano, and L. Brandt, The effect of particle density in turbulent channel flow laden with finite size particles in semi-dilute conditions, *Phys. Fluids* **28**, 033301 (2016).
- [20] N. Nangia, N. A. Patankar, and A. P. S Bhalla, A DLM immersed boundary method based wave-structure interaction solver for high density ratio multiphase flows, *J. Comput. Phys.* **398**, 108804 (2019).
- [21] F. Picano, W.-P. Breugem, and L. Brandt, Turbulent channel flow of dense suspensions of neutrally buoyant spheres, *J. Fluid Mech.* **764**, 463 (2015).
- [22] M. E. Rosti, M. N. Ardekani, and L. Brandt, Effect of elastic walls on suspension flow, *Phys. Rev. Fluids* **4**, 062301 (2019).
- [23] M. E. Rosti and L. Brandt, Suspensions of deformable particles in a Couette flow, *J. Non-Newtonian Fluid Mech.* **262**, 3 (2018).
- [24] N. Sharma and N. A. Patankar, A fast computation technique for the direct numerical simulation of rigid particulate flows, *J. Comput. Phys.* **205**, 439 (2005).
- [25] M. Uhlmann, An immersed boundary method with direct forcing for the simulation of particulate flows, *J. Comput. Phys.* **209**, 448 (2005).
- [26] M. Uhlmann and T. Doychev, Sedimentation of a dilute suspension of rigid spheres at intermediate Galileo numbers: The effect of clustering upon the particle motion, *J. Fluid Mech.* **752**, 310 (2014).
- [27] E. Climent and M. R. Maxey, Numerical simulations of random suspensions at finite Reynolds number, *Int. J. Multiphase Flow* **29**, 579 (2003).
- [28] A. A. Howard, M. R. Maxey, and K. Yeo, Settling of heavy particles in concentrated suspensions of neutrally buoyant particles under uniform shear, *Fluid Dyn. Res.* **50**, 041401 (2018).
- [29] K. Gudmundsson and A. Prosperetti, Improved procedure for the computation of Lamb's coefficients in the Physalis method for particle simulation, *J. Comput. Phys.* **234**, 44 (2013).
- [30] A. J. Sierakowski and A. Prosperetti, Resolved-particle simulation by the physalis method: Enhancements and new capabilities, *J. Comput. Phys.* **309**, 164 (2016).
- [31] Y. Wang, A. Sierakowski, and A. Prosperetti, Fully resolved simulation of particulate flows with particles-fluid heat transfer, *J. Comput. Phys.* **350**, 638 (2017).
- [32] D. Willen and A. Prosperetti, Resolved simulations of sedimenting suspensions of spheres, *Phys. Rev. Fluids* **4**, 014304 (2019).
- [33] S. Kim and S. J. Karrila, *Microhydrodynamics: Principles and Selected Applications* (Butterworth-Heinemann, Boston, MA, 1991; reprinted by Dover, New York).
- [34] H. Lamb, *Hydrodynamics*, 6th ed. (Cambridge University Press, Cambridge, UK, 1932; reprinted by Dover, New York).

- [35] A. J. Sierakowski, Numerical simulation of disperse particle flows on a graphics processing unit, Ph.D. thesis, Johns Hopkins University, 2016.
- [36] J. A. Simeonov and J. Calantoni, Modeling mechanical contact and lubrication in direct numerical simulations of colliding particles, *Int. J. Multiphase Flow* **46**, 38 (2012).
- [37] C. T. Crowe, J. D. Schwarzkopf, M. Sommerfeld, and Y. Tsuji, *Multiphase Flows with Droplets and Particles*, 2nd ed. (CRC Press, Boca Raton, FL, 2012).
- [38] D. Willen, A. J. Sierakowski, G. Zhou, and A. Prosperetti, Continuity waves in resolved-particle simulations of fluidized beds, *Phys. Rev. Fluids* **2**, 114305 (2017).
- [39] N. V. Brilliantov and T. Pöschel, *Kinetic Theory of Granular Gases* (Oxford University Press, Oxford, UK, 2004).
- [40] T. P. C. van Noije and M. H. Ernst, Velocity distributions in homogeneous granular fluids: The free and the heated case, *Granular Matter* **1**, 57 (1998).
- [41] D. M. Kalyon, Apparent slip and viscoplasticity of concentrated suspensions, *J. Rheol.* **49**, 621 (2005).
- [42] M. N. Ardekani, O. Abouali, F. Picano, and L. Brandt, Heat transfer in laminar Couette flow laden with rigid spherical particles, *J. Fluid Mech.* **834**, 308 (2018).
- [43] G. Drazer, J. Koplik, B. Khusid, and A. Acrivos, Deterministic and stochastic behavior of non-Brownian spheres in sheared suspensions, *J. Fluid Mech.* **460**, 307 (2002).
- [44] G. Zhou and A. Prosperetti, Lamb's solution and the stress moments for a sphere in Stokes flow, *Eur. J. Mech. B/Fluids* **79**, 270 (2019).
- [45] G. K. Batchelor, The stress system in a suspension of force-free particles, *J. Fluid Mech.* **41**, 545 (1970).
- [46] S. Gallier, E. Lemaire, F. Peters, and L. Lobry, Rheology of sheared suspensions of rough frictional particles, *J. Fluid Mech.* **757**, 514 (2014).
- [47] E. Guazzelli, and O. Pouliquen, Rheology of dense granular suspensions, *J. Fluid Mech.* **852**, P1 (2018).
- [48] I. M. Krieger, Rheology of monodisperse lattices, *Adv. Colloid Interface Sci.* **2**, 111 (1972).
- [49] F. Picano, W.-P. Breugem, D. Mitra, and L. Brandt, Shear Thickening in Non-Brownian Suspensions: An Excluded Volume Effect, *Phys. Rev. Lett.* **111**, 098302 (2013).
- [50] C. Gamonpilas, J. F. Morris, and M. M. Denn, Shear and normal stress measurements in non-Brownian monodisperse and bidisperse suspensions, *J. Rheol.* **60**, 289 (2016).
- [51] C. Gamonpilas, J. F. Morris, and M. M. Denn, Erratum: "Shear and normal stress measurements in non-Brownian monodisperse and bidisperse suspensions" [J. Rheol. 60(2), 289-296 (2016)], *J. Rheol.* **62**, 665 (2018).
- [52] R. Seto and G. G. Giusteri, Normal stress differences in dense suspensions, *J. Fluid Mech.* **857**, 200 (2018).
- [53] R. Mari, R. Seto, J. F. Morris, and M. M. Denn, Shear thickening, frictionless and frictional rheologies in non-Brownian suspensions, *J. Rheol.* **58**, 1693 (2014).
- [54] I. R. Peters, S. Majumdar, and H. M. Jaeger, Direct observation of dynamic shear jamming in dense suspensions, *Nature* **532**, 214 (2016).
- [55] Q. Xu, S. Majumdar, E. Brown, and H. M. Jaeger, Shear thickening of highly viscous granular suspensions, *Europhys. Lett.* **107**, 68004 (2014).
- [56] G. Drazer, J. Koplik, B. Khusid, and A. Acrivos, Microstructure and velocity fluctuations in sheared suspensions, *J. Fluid Mech.* **511**, 237 (2004).